Journal of Energy Storage 69 (2023) 107921

Contents lists available at ScienceDirect

Journal of Energy Storage

journal homepage: www.elsevier.com/locate/est

Research papers

The effect of hot wall configuration on melting flow of nano-enhanced phase change material inside a tilted square capsule

Nidhal Ben Khedher [a,b], Mikhail Sheremet [c], Amira M. Hussin [d], S.A.M. Mehryan [e,*], Mohammad Ghalambaz [c,*]

[a] Department of Mechanical Engineering, College of Engineering, University of Ha'il, P.O. Box 2440, Ha'il City, Saudi Arabia
[b] Laboratory of Thermal and Energetic Systems Studies (LESTE) at the National School of Engineering of Monastir, University of Monastir, 50000, Tunisia
[c] Laboratory on Convective Heat and Mass Transfer, Tomsk State University, Tomsk, Russia
[d] Department of Mathematics, Al-Aflaj College of Science and Humanities, Prince Sattam bin Abdulaziz University, Al-Aflaj 710-11912, Saudi Arabia
[e] Young Researchers and Elite Club, Yasooj Branch, Islamic Azad University, Yasooj, Iran

ARTICLE INFO

Keywords:
Hot wall configuration
Nano-enhanced phase change material
Tilted square capsule
Porosity-enthalpy technique
Melting

ABSTRACT

The aim of this study is to investigate the influence of the hot wall configuration on the thermal performance of an inclined square capsule containing the nano-enhanced phase change material (NePCM). The porosity-enthalpy technique is used to track the melting flow. The correctness of the obtained numerical results is verified through the experimental data from the literature. Three different configurations for the hot wall of the tilted square capsule are considered. For the square capsule heated from the side wall, the inclination angle of 85° shows the maximum charging power while the minimum charging power occurred at 5°. The charging power for the optimum angle (85°) was 16 % higher than that of 5°. For the enclosure equally heated from the side wall and bottom, the inclination angles of 25° and 65° provide the maximum charging power. Moreover, an enclosure mostly heated from the side wall (2/3) and partially heated from the bottom (1/3), produces the maximum charging power at 25°. The results also indicate that GNPs with 1 % wt produce the maximum charging power.

1. Introduction

Phase change materials (PCMs), which can absorb, store and release large amounts of thermal energy, are used in a wide range of applications from buildings to electronics to store energy as well as prevent temperature fluctuations. Using the thermal energy storage systems (TES), which utilize the PCMs is known as an effective pattern to conserve available energy and bettering its utilization. Hence, the use of appropriate systems can reduce the mismatch between energy supply and demand. The high energy storage density of PCMs has made them a research topic of interest to numerous researchers. To this date, a large number of studies have been conducted to investigate the utilization of PCMs in different fields. Building energy conservation [1], electronic cooling [2,3], battery thermal management systems [4–6], and solar energy storage [7,8] are among the applications of PCMs.

Zhou et al. [9] analyzed the influencing factors in Phase Change Material Wallboard (PCMW) parametrically. They numerically studied the impacts of the thermal properties of the interior and exterior PCMWs on their thermal performance. In their work, fusion temperature, melting range, latent heat, thermal conductivity and surface heat transfer coefficient were considered as the influencing parameters on the thermal performance of the PCMWs. Jaworski [10] studied the thermal performance of a PCM-based heat spreader for electronic cooling. The author proposed a new pin-fin radiator in which the PCM filled the pins. The results showed that the high heat transfer surface and high thermal capacity could effectively remove the heat from the electronic equipment. Mousavi et al. [11] proposed a new design for the battery thermal management system based on the PCM and mini channel. In this new design, the cold plates were filled with n-eicosane as the PCM. The maximum temperature of the battery module with the cold plates and the PCM is 10.5 K less than that of the pack with only cold plates.

Many studies with different strategies have sought to find energy storage systems with the best performance. These strategies include the use of metal fins [12–14], porous metal foams [15–17], and high-conductivity nanoparticles [18–20]. Ji et al. [14] proposed the use of inclined fins to suppress the non-uniform heat flux, and consequently, increase the melting rate of the PCM. In this study, the fins with the

* Corresponding authors.
E-mail addresses: n.khedher@uoh.edu.sa (N.B. Khedher), sheremet@math.tsu.ru (M. Sheremet), alal171366244@gmail.com (S.A.M. Mehryan), m.ghalambaz@gmail.com (M. Ghalambaz).

https://doi.org/10.1016/j.est.2023.107921
Received 19 February 2023; Received in revised form 4 May 2023; Accepted 2 June 2023
Available online 8 June 2023

Nomenclature

Latin symbols

a(T)	ramp function
A_m	mushy region morphology constant (kg m^{-3} s^{-1})
C_p	sensible heat capacity (J kg^{-1} K^{-1})
f_b	buoyancy force (N m^{-3})
f_m	damping force (N m^{-3})
g	gravity (m s^{-2})
k	thermal conductivity (W m^{-1} K^{-1})
p	pressure (N m^{-2})
T	temperature (K)
t	time (s)
u	velocity component in x direction (m s^{-1})
v	velocity component in y direction (m s^{-1})
wt	weight fraction of the nanoparticles
x	x coordinate (m)
y	y coordinate (m)

Greek symbols

β	volume thermal expansion (K^{-1})
Δ	gradient
μ	dynamic viscosity (kg m^{-1} s^{-1})
η	inclination angle of cavity
ρ	density (kg m^{-3})

Subscript

f	fusion
h	hot
i	coordinate
initial	initial condition

inclination angles of −30°, −15°, 0.0°, +15°, and + 30° were studied. It was found that the fin at a downward angle of −15° shows the best performance compared to the other configurations. Kalbasi et al. [21] analyzed the optimum fins number in a heat sink filled with the PCM. The results indicated that the optimum number of fins is reduced with an increment in the fin thickness. Also, it was found that the optimal number of fins is less for the heat sink with higher height. Mahdi et al. [22] used a cascaded metal foam to enhance the heat transfer in a shell and tube TES system. The numerical results showed that the energy recovery and storage times are significantly reduced using the composite's porosity-cascaded metal foam.

The inclination of a cavity can have a significant effect on the melting behavior of a PCM placed inside it. Therefore, it is important to consider the inclination angle of the cavity when designing systems that use PCMs to ensure optimal melting performance. A numerous studies have investigated the effect of cavity inclination on the melting behavior of PCMs under different conditions [23–26]. Yazici et al. [23] experimentally studied the combined influence of the tilted angle and fin number on the cooling effectiveness of a heat sink filled with N-eicosane. The report reveals that the heat sink having an inclination angle of $\pi/3$ and three fins has the best performance in terms of working time. Siyabi et al. [25] conducted a study on the melting behavior of a cylindrical thermal storage system using paraffin wax as the phase change material at different inclination positions. They used both experimental and numerical approaches to analyze the temperature distribution, melting profiles, stored heat rate, and liquid PCM flow within the storage. The study found that the inclination angle had a significant impact on the melting characteristics, with the 45° inclination angle having the fastest melting rate. An experimental study by Korti and Guellil [27] investigated the melting behavior of a PCM (paraffin with the melting range of 49–54 °C) inside a square cavity that was inclined at angles ranging from 0° to 90°. The PCM was heated from one side using a constant heat flux. The study found that the melting rate of the PCM augmented with increasing cavity inclination, with the highest melting rate observed at an inclination angle of 45°.

Huang et al. [26] numerically studied the effect of the inclination angle of a porous rectangular capsule on the dynamic behavior of phase change of a PCM. They reported that the melting time of the PCM could be shortened by using a porous medium with smaller pore density and a larger Rayleigh number. Kamkari et al. [28] conducted an investigation into the melting behavior of a high Prandtl number PCM, within a rectangular enclosure that is heated from one side while the remaining walls are thermally insulated. To observe the dynamic thermal behavior of the PCM melting, the experiments were conducted using different hot wall temperatures and inclination angles. The outcomes demonstrated that lowering the inclination angle from 90° to 0° results in an increase in convection currents and the appearance of chaotic flow structures. Keeping the hot wall temperatures constant, decreasing the inclination angle results in a significant increase in the amount of energy transferred from the enclosure's hot wall to the PCM.

In many systems, the presence of nanoparticles can enhance the performance of the system [29–31]. Since nano-enhanced PCM can remove one of the key barriers to the use of PCMs, it has attracted increasing attention. Pahamli et al. [32] studied the melting behavior of a PCM in a shell and tube heat exchanger through experimental and numerical methods. The study explores the effects of two parameters: adding nano-additives and changing the inclination angle. The incorporation of nanoparticles in PCM improves thermal conductivity, resulting in faster melting rates at the bottom of the heat exchanger. Increasing the inclination angle also accelerates the melting process at higher attitudes, reducing the total melting time. The simultaneous use of NePCM and increased inclination angle leads to enhanced natural convection and thermal conductivity, improving the melting process of NePCM. Shahabadi et al. [33] studied the melting flow of a nano-enhanced PCM (NePCM), including the graphite nanoplates (GNPs) in a semi-elliptical capsule. It is found that the capsule with the nanoplates mass fraction of 1.0 % shows the highest performance, which is 7.2 % more compared to the pure PCM. Moreover, they showed that an angular deviation of semi-elliptical capsule from the horizontal form increases the melting time, and consequently, decreases the thermal performance.

Li et al. [34] studied the effect of adding graphene nanoplatelets to 1-Tetradecanol PCM on melting heat transfer in a differentially-heated rectangular cavity. The results showed that increasing the graphene nanoplatelets loading leads to a deceleration in both heat storage and transfer rates during melting, likely due to the increase in viscosity. The study conducted by Chamkha et al. [35] was concerned with exploring the process of how a PCM that has been modified with nanoparticles melts in a square-shaped container. The container has a heated cylinder in the middle, and during the melting process, both single and hybrid types of nanoparticles are present. The study's findings reveal that the rate at which the material melts is considerably higher when the Fourier number fluctuates between 0 and 0.5. However, a subsequent increase in the Fourier number causes a decrease in the rate of melting. Mehryan et al. [36] devoted a work to an opportunity to use NePCM for an intensification of heat removal within a gap between two coaxial vertical isothermal cylinders. The power-law model was used for the description of the non-Newtonian behavior of the NePCM. It is found that adding nanoparticles of $MPSiO_2$ to the PCM results in a slower melting process and a decrease in the average Nusselt number.

Although many studies have investigated the effect of tilting of PCM containers on system performance, no study has been conducted on the

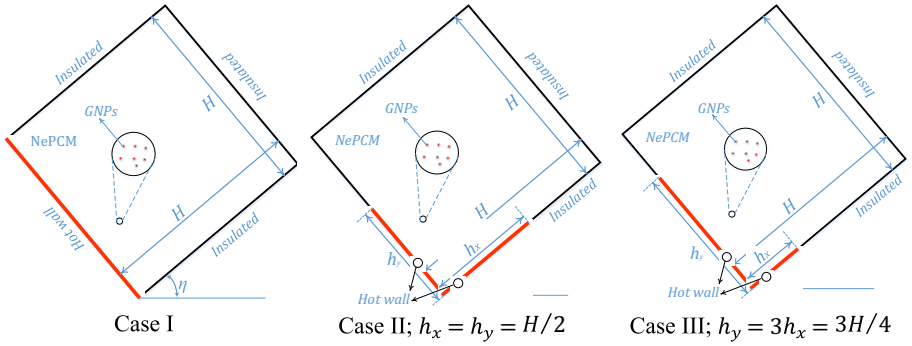

Fig. 1. Graphical view of the subject along with the hot wall configurations.

Table 1
Thermophysical specifications of the NePCM samples at various loading of GNPs [37].

Characteristics	0 wt%	0.5 wt%	1 wt%	3 wt%
Thermal expansion coefficient, β ($1\ K^{-1}$)	0.001018	0.001018	0.001008	0.000987
Density (solid)	891.4	894.1	896.9	907.9
Density (liquid)	821.6	824.3	826.9	837.6
Thermal conductivity (solid)	0.252	0.350	0.451	0.540
Thermal conductivity (liquid)	0.159	0.180	0.260	0.320
Dynamic viscosity	13.23	23.45	59.5	194.01
Specific heat capacity (solid)	2040	2020	1990	1910
Specific heat capacity (liquid)	2360	2330	2300	2190
Melting point	37	37	37	37
Latent heat	227.8	219.5	212.2	183.5

influence of the hot walls configuration on the effectiveness of TES systems. Hence, in this work, as the first work, the configuration effect of the hot walls of an inclined capsule is explored on the thermal performance. Moreover, the experimental data is employed to study the impacts of GNPs additives on the system performance.

2. Mathematical formulation

Fig. 1 illustrates a square enclosed medium with three hot-wall configurations saturated with a NePCM. As shown, the enclosure with the size of 40 mm is tilted with an angle of η relative to the horizontal axis. The present design configuration is important in a stack of PCM channels (PCM containers) where the heat transfer fluid moves between the channels. The heat transfer between the PCM and heat transfer fluid occurs through the container wall exposed to the heat transfer fluid. The used PCM is 1-Tetradecanol, and the added nano-particle is graphite nanoplatelets (GNPs). The thermophysical specifications of the NePCM for different mass fractions of the nanoplates are used based on the experimental data [37] and tabulated in Table 1. The considered assumptions for modeling the NePCM melting process are listed as the following:

- The volume change of the NePCM during melting can be ignored.
- The NePCM contains a homogeneous dispersion of nanoparticles.
- There is no sedimentation and accumulation of the nano-additives.

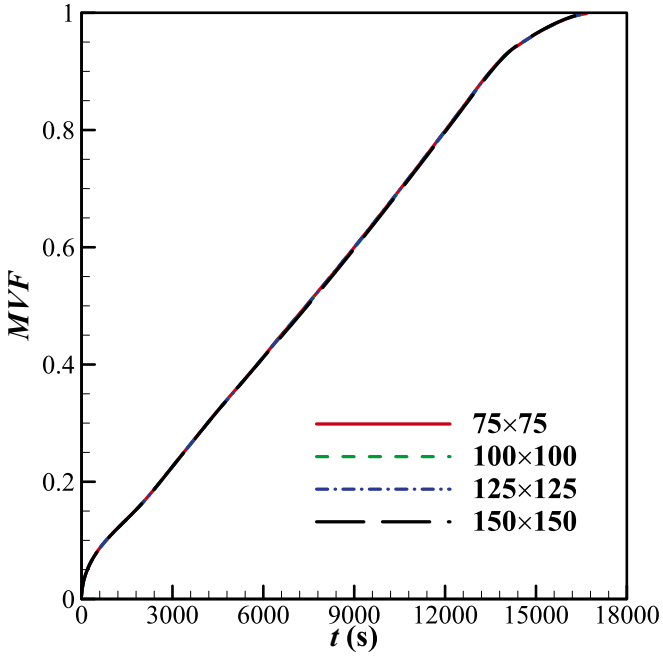

Fig. 2. Mesh sensitivity analysis.

- The Boussinesq linear approximation is used to model the gravity force in momentum equations.

The flow NePCM is modeled by using the enthalpy-porosity formulation. By applying the above-mentioned considerations, the governing equations are:

I) Continuity

$$\frac{\partial u_i}{\partial x_i} = 0 \tag{1}$$

II) Momentum conservation

$$\rho_{LNePCM}\left(\frac{\partial u_i}{\partial t} + u_j\frac{\partial u_i}{\partial x_j}\right) = -\frac{\partial p}{\partial x_i} + \mu_{LNePCM}\frac{\partial^2 u_i}{\partial x_i x_j} + f_{b_i} + f_{m_i} \tag{2}$$

in which i can be 1 or 2. 1 and 2 denote to the x and y coordinates. Moreover, $u_1 = u$ and $u_2 = v$. f_{m_i} is defined as the following:

$$f_{m_i} = -\frac{A_m(1-a(T))^2}{a^3(T)+\epsilon}u_i \tag{3}$$

where $A_m = 5 \times 10^5$ and $\epsilon = 10^{-3}$. $a(T)$ is a ramp function, given by:

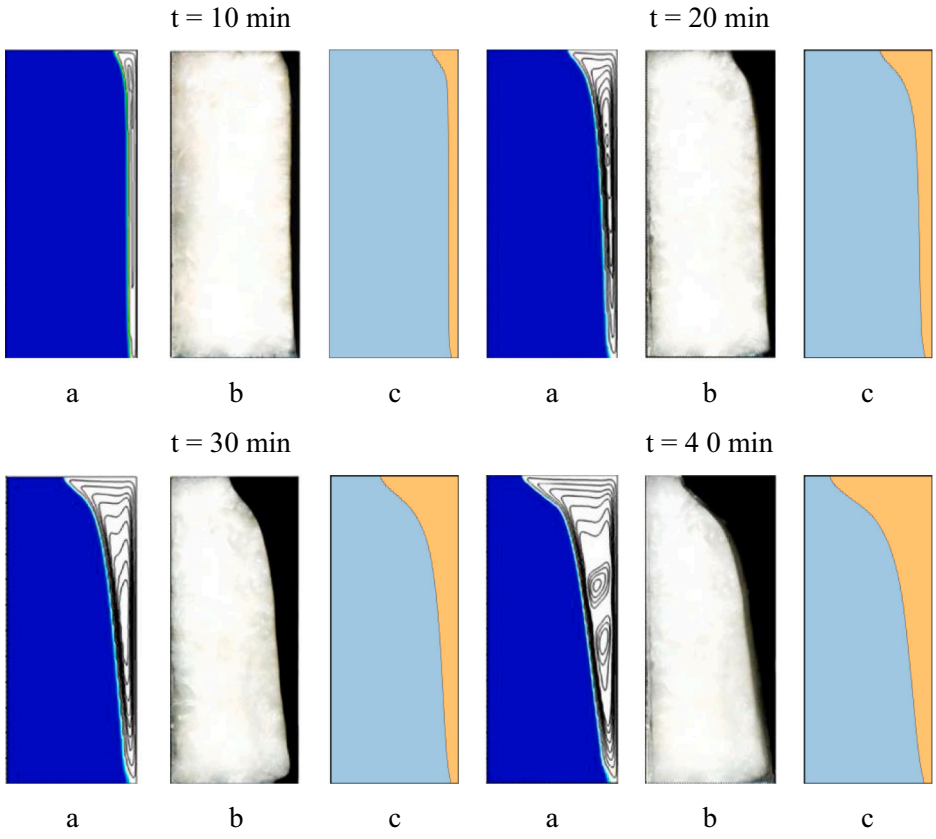

Fig. 3. Comparison between the melting fields available in [38] and those obtained by the present study; a: numerical results [38], b: experimental results in [38], and c: the present study.

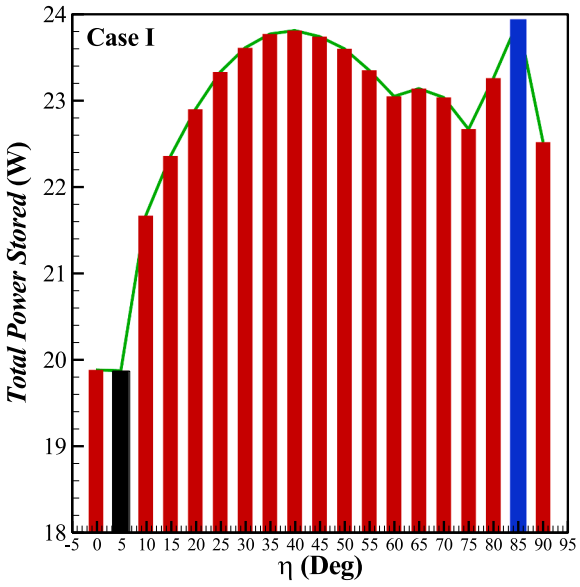

Fig. 4. Effect of inclination angle on Case I: The blue bar is the maximum, and the black bar is the minimum. (For interpretation of the references to colour in this figure legend, the reader is referred to the web version of this article.)

$$a(T) = \begin{cases} 0 \; T < T_f - \Delta T_f/2 \\ \dfrac{T - T_f}{\Delta T_f} + \dfrac{1}{2} \; T_f - \Delta T_f \Big/ 2 < T < T_f + \Delta T_f \Big/ 2 \\ 1 \; T > T_f + \Delta T_f/2 \end{cases} \tag{4}$$

f_{b_i} of Eq. (2) is:

$$f_{b_i} = \rho_{LNePCM}\beta_{LNePCM}(T - T_f)g_i = \rho_{LNePCM}\beta_{LNePCM}(T - T_f)\begin{cases} gsin\eta \; i = 1 \\ gcos\eta \; i = 2 \end{cases} \tag{5}$$

III) Energy conservation

$$\rho_{NePCM}C_{p,NePCM}\frac{\partial T}{\partial t} + \rho_{LNePCM}C_{p,LNePCM}u_i\frac{\partial T}{\partial x_i} = \frac{\partial}{\partial x_i}\left(k_{NePCM}\frac{\partial T}{\partial x_i}\right) + \rho_{NePCM}L_{NePCM}\frac{\partial a(T)}{\partial t} \tag{6}$$

in which,

$$k_{NePCM} = k_{SNePCM} + a(T)(k_{LNePCM} - k_{SNePCM}) \tag{7}$$

$$\rho_{NePCM} = \rho_{SNePCM} + a(T)(\rho_{LNePCM} - \rho_{SNePCM}) \tag{8}$$

$$\rho_{NePCM}C_{p,NePCM} = \rho_{SNePCM}C_{p,SNePCM} + a(T)\left(\rho_{LNePCM}C_{p,LNePCM} - \rho_{SNePCM}C_{p,SNePCM}\right) \tag{9}$$

The temperature on the hot walls is fixed at $T_h = 47°C$, and the other walls are well insulated. Also, considering the no-slip boundary conditions on the stationary walls, the velocity on the walls is zero. The initial temperature of the NePCM is $T_{initial} = 27°C$.

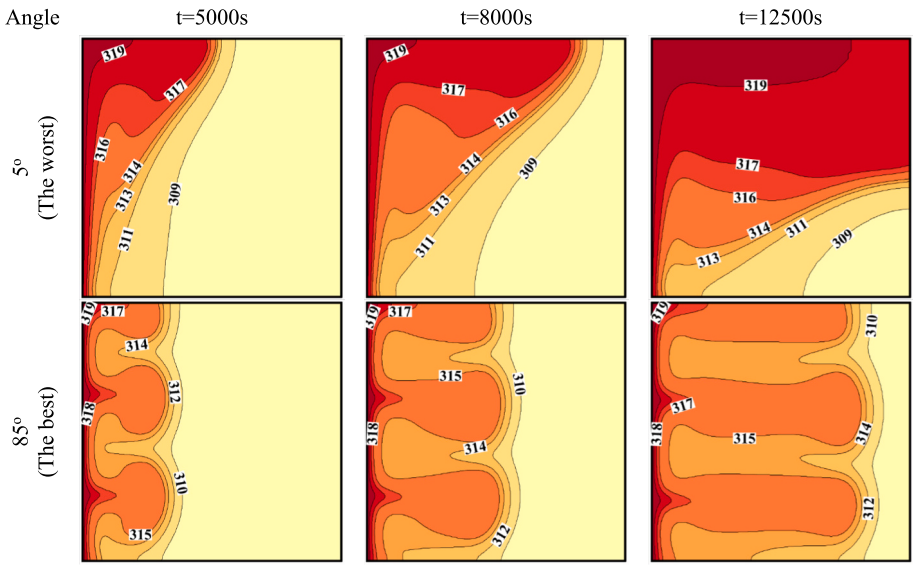

Fig. 5. Contours of isotherm for the best and worst results raised from Case I.

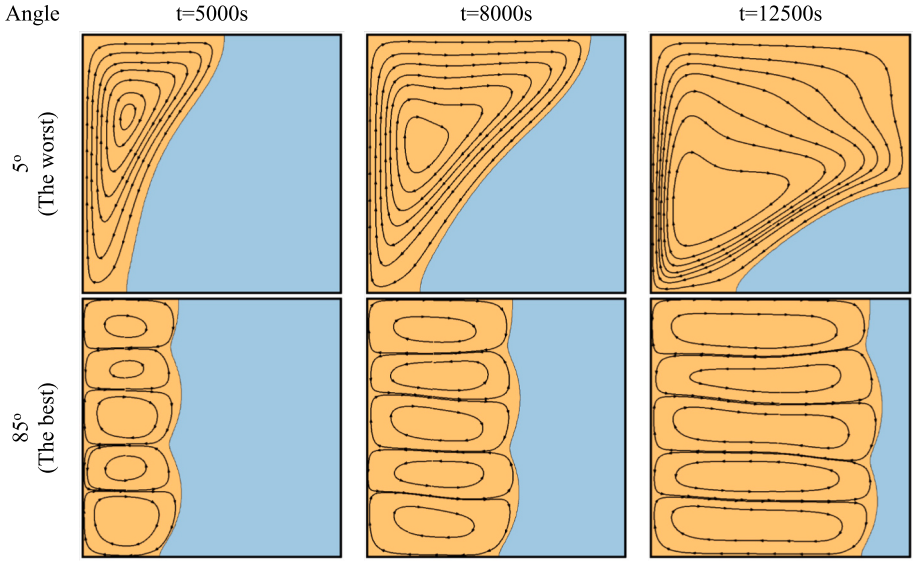

Fig. 6. Streamlines for the best and worst results raised from Case I.

3. Numerical approach, grid sensitivity analysis, and validation/verification

The Finite Element Method (FEM) is utilized to integrate the equations of the model. The FEM is based on a weighted residual approach that involves the transformation of partial differential equations that govern the conservation of mass, momentum, and energy into a weak form. This weak form is then integrated over mesh elements to reach the residual equation. The field variables were iteratively solved by applying the residual equations. The convergence was aimed to be improved by setting a damping factor of 0.8. To preserve a relative solution accuracy below 10E-4, the time step was managed by utilizing the backward differential formula with a free order between 1 and 2.

A structured mesh with uniform cell sizes was utilized to discretize the governing equations across the solution domain. Grid study, also known as grid convergence study, is a systematic analysis performed to evaluate the accuracy and reliability of numerical simulations or computational models by investigating the effect of grid resolution on the results. The grid study involves running a series of simulations with different grid sizes while keeping all other parameters constant. The results obtained from these simulations are then compared to determine the degree of convergence and establish the minimum grid size required to obtain accurate and reliable results. Fig. 2 demonstrates the effect of the number of elements on the accuracy of the results. To balance between the computational cost and the accuracy of the results, a network with a size of 100 × 100 is chosen.

To verify the numerical simulation in this study, the melting fields obtained were compared to both the numerical and experimental fields reported in [38]. In the computational domain of Ref [38], a rectangular enclosure with a width of 5 cm and a height of 12 cm was filled with lauric acid as the PCM. The right wall of the enclosure was maintained at a temperature of 70 °C, while the other walls were insulated. As shown in Fig. 3, the results of this study were found to be in excellent agreement with those presented in [38].

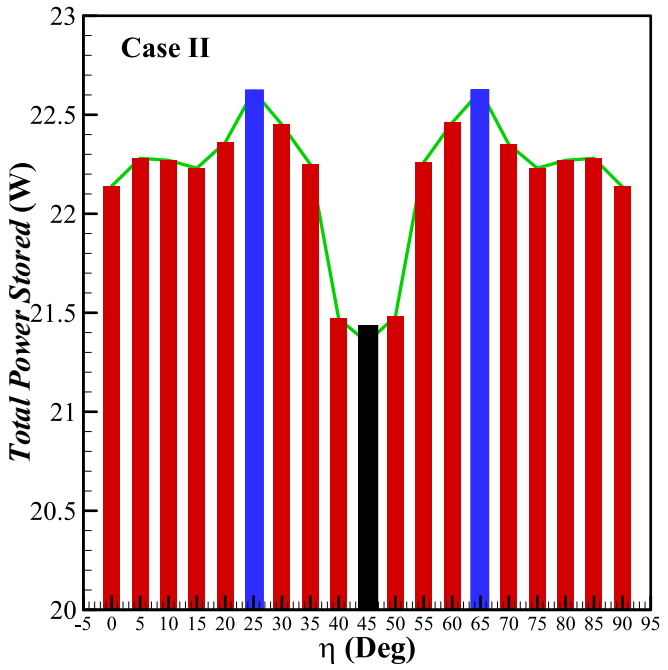

Fig. 7. Effect of inclination angle on Case II: The blue bar is the maximum, and the black bar is the minimum. (For interpretation of the references to colour in this figure legend, the reader is referred to the web version of this article.)

4. Results and discussion

In the present work, the influence of angel inclination of the enclosure ($0 \leq \eta \leq 90°$) and the mass fraction of the GNP additives ($0\ \% \leq wt \leq 3\ \%$) were addressed on the melting heat transfer isotherms, streamlines for the three boundary configurations.

Fig. 4 illustrates the impact of inclination angles on the energy storage power for Cases I heated boundary configurations. The results were reported for a fixed mass concentration of 1 % GNP additives. Fig. 4 shows the maximum power obtained at an inclination angle of 85° for a cavity heated just from the side wall (Case I). The increase of inclination angle from 0 to 45° increases the thermal charging power. A further increase of the inclination angle beyond 45° reduces the thermal charging power. A sharp rise of storage power commences at $\eta = 75°$ and reaches maximum power at $\eta = 85°$ with a thermal energy storage magnitude of 23.9 W.

Considering Case I configuration, Figs. 5 and 6 provide a visual depiction of a typical melting front for Cases $\eta = 5°$ and $\eta = 85°$, which correspond to the worst and best thermal powers, respectively. The behavior displayed in the case of $\eta = 5°$ draws parallels to the process of melting heat transfer within an enclosure that's warmed from its left vertical wall. However, there is a 5° gap to a fully horizontal heated wall. In this instance, the heated, molten PCM is propelled toward the top of the capsule, eventually making contact with the melting front. The heated liquid adjacent to the vertical wall ascends and extends toward the topmost regions. It then absorbs the latent heat from the solid PCM, leading to a drop in its temperature.

Consequently, the now-cooled liquid descends, reaching the bottommost regions and the heated wall. This cycle of flow circulation is completed in this manner. This pattern of circulation aligns with the streamline patterns illustrated in Fig. 6. Therefore, the topmost region of the melting front advances toward the solid regions faster than the bottom. This is because the heated liquid first reaches the top due to natural convection flows. However, in the case of $\eta = 85°$, the shape of the melting interface diverges from the previous case.

The shape here closely resembles a scenario where melting originates from below. This is because, in this instance, gravity is almost perpendicular to the heated wall. Under such circumstances, the hot liquid parcels are confined next to the heated wall, striving to move against gravity toward the colder PCM. Simultaneously, the cold liquid parcels, positioned near the melting interface, also strive to move in the direction of the heated wall in alignment with the vector of gravity. Both hot and cold parcels exert pressure on each other until they find a way to converge. This dynamic scenario leads to the formation of Benard-shaped cells, which intermittently inject cold and hot liquid parcels toward the melting interface and the heated wall. As a result, the isotherms form plume-shaped patterns directed toward the melting interface. In this case, the shape of the melting interface is almost uniform and parallel to the heated wall. It progresses in a direction that is perpendicular to the heated wall, setting this case apart from the one with $\eta = 5°$.

Attention to Fig. 4 shows that a fully horizontal heated wall would

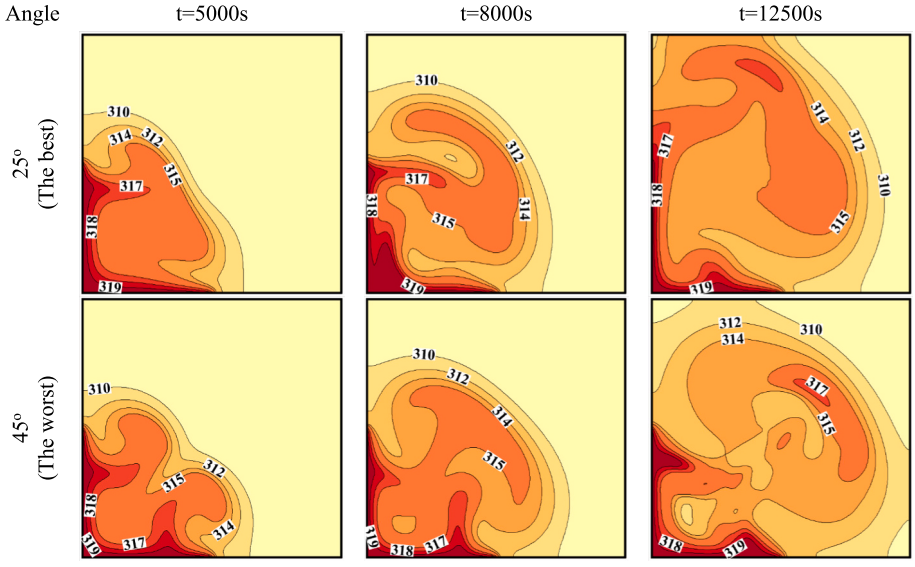

Fig. 8. Contours of isotherm for the best and worst results raised from Case II.

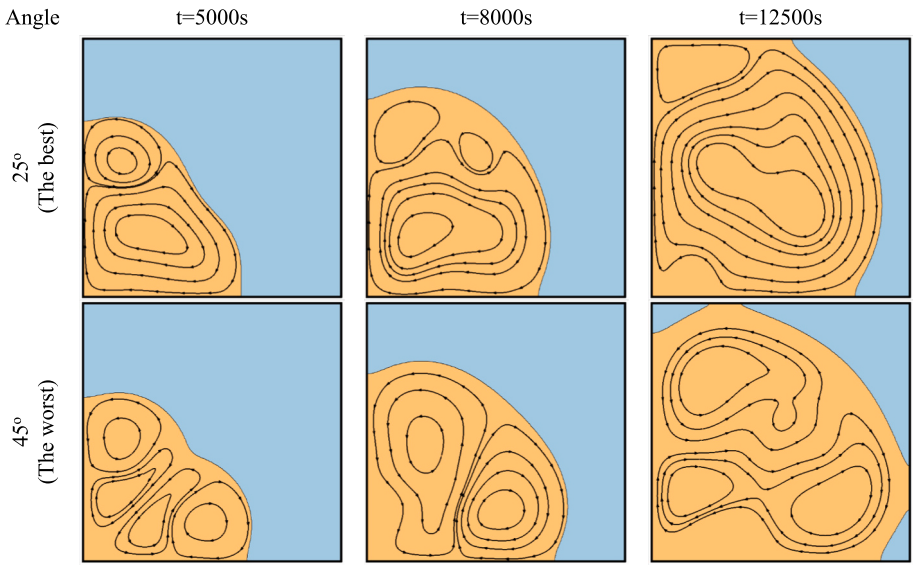

Fig. 9. Streamlines for the best and worst results raised from Case II.

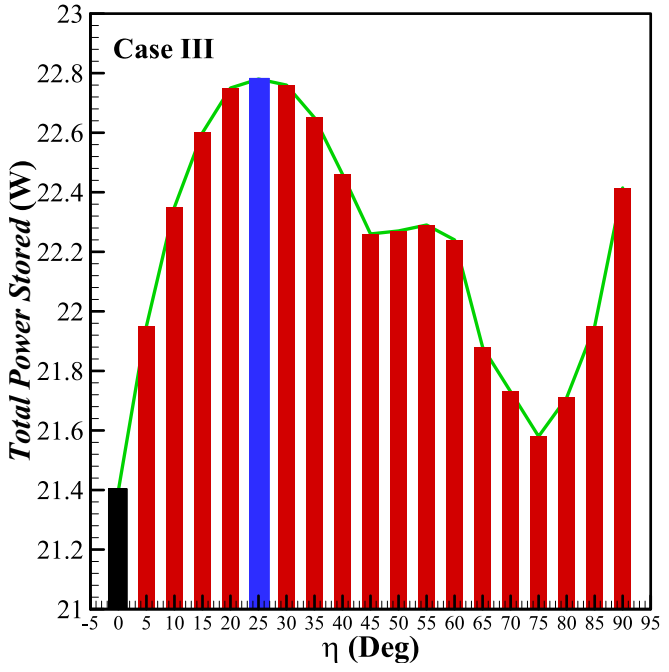

Fig. 10. Effect of inclination angle on Case III: The blue bar is the maximum, and the black bar is the minimum. (For interpretation of the references to colour in this figure legend, the reader is referred to the web version of this article.)

lower charging power. There is a 5° gap difference between the fully horizontal heated wall ($\eta = 90°$) and optimum case $\eta = 85°$. This small gap adds a slight slope to the enclosure and guides the heated packets in a direction along the heated wall, and boosts the heat transfer rate. The heated packets charge toward the melting front for a case heated from below. However, this slight slope would help the heated thermal packets charge faster toward the melting front.

Fig. 7 presents a compelling visualization of power storage for Scenario II. In this scenario, the compartment experiences equal heat from both the vertical and horizontal surfaces. Notably, there is a substantial decrease in power around the 45° mark, characterized by symmetrical and consistent heating in the vertical direction. Illustrations of the isotherms and streamlines for this particular case are provided in Figs. 8 and 9.

In this configuration, melting initiates at the thermally stimulated corner of the compartment, progressively moving toward the opposite corner. The streamlines, however, display a contradictory pattern. During the initial phase of thermal charging (at $t = 5000$ s), numerous faint circulation currents are observable within the liquid area, which is restricted to the heated sections of the walls. Over time, these currents amalgamate, eventually resulting in two dominant circulatory flows at $t = 8000$ s and $t = 12{,}500$ s.

One of these currents initiates from the heated lower surface, moving toward the melting front, while the other begins at the vertically heated surface, also progressing toward the melting front. When these two currents meet in the center, they cause a weakening in the overall melting process and power charging due to the resulting pattern of flow circulations.

Fig. 9 also reveals two optimal inclination angles, 25° and 65°, for this scenario. Indeed, the physical configuration of Scenario II is symmetrical to 45°. This behavioral trend is evident in Fig. 7. For our purposes, $\eta = 25°$ was chosen as the best case, with its corresponding isotherm and streamlines displayed in Figs. 8 and 9. At the angle of 25°, the molten region is dominated by a primary circulatory flow, originating from the heated surfaces and extending to the melting front. This primary circulation boosts natural convection heat transfer, thereby augmenting the enclosure's TES power.

Fig. 10 shows that the minimum storage power takes place at the zero-inclination angle, and the maximum power occurs at $\eta = 25°$ for Case III. The corresponding isotherms and streamlines for these two cases are depicted in Figs. 11 and 12. It should be noted that the heating boundary condition, as shown in Fig. 1, is already nonsymmetric. 2/3 of the vertical wall and 1/3 of the bottom wall are heated.

The isotherms (Fig. 11) for $\eta = 0$ show that the molten liquid is heated at a small portion at the bottom and creates a natural convection flow (Fig. 12) which continues over the heated part of the wall toward the top and then reaches the melting front. The heating part of the wall at the bottom fairly pushes the melting front toward the solid region; hence, an almost uniform vertical melting front can be seen at $t = 5000$ s. After a while ($t = 8000$ s and 12,500 s), the distance of the melting front from the heated wall increases, and consequently, its impact on the melting front also diminishes. Thus, the shape of the melting front returns to its typical dome shape at the final stages of melting.

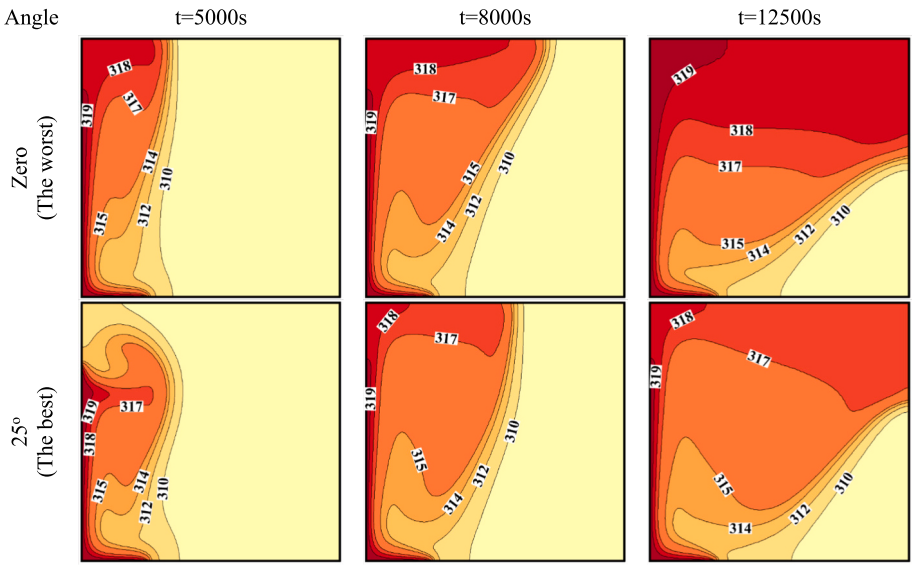

Fig. 11. Contour of isotherm for the best and worst results raised from Case III.

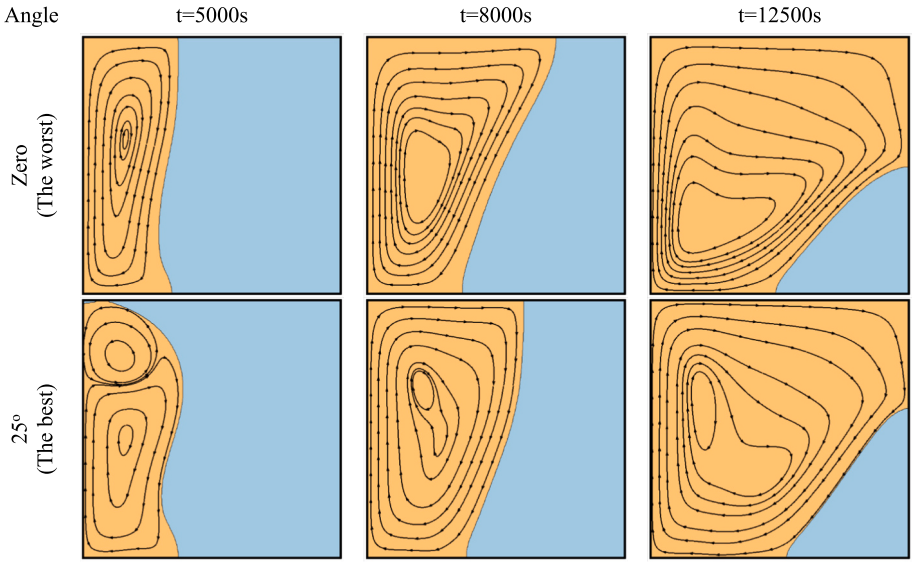

Fig. 12. Streamlines for the best and worst results raised from Case III.

The isotherms (Fig. 11) for $\eta = 25°$ show the creation of Benard cells at the early stages of melting ($t = 5000$ s), but the cells are not uniform. There is a combination of Benard shape cells at the top and typical natural convection from the bottom. The streamlines (Fig. 12) also confirm the presence of two circulation flows, one at the bottom and another at the top. After a while ($t = 8000$ s), the Benard cells vanished, and a large circulation flow formed in the molten region (Fig. 14). This circulation flow effectively targets the solid region at the end of the melting process, resulting in optimum charging power.

Fig. 13 provides a comparative analysis of the energy storage across all cases under consideration. This figure highlights the maximum and minimum charging powers via blue and black bars, respectively. Upon examination, it is apparent that the maximum global power is attributed to Case I, where the inclination angle, η, is 85°. This is followed by Case III and Case II, each with their maximum power occurring at $\eta = 25°$ and $\eta = 25°$ or 65° respectively.

Intriguingly, Case I, with an inclination angle of $\eta = 5°$, exhibits the minimum power, followed by the other scenarios. As a result, Case I emerges as the most fitting for static storage applications, where the inclination angle can be maintained at an optimal value. In contrast, Cases II and III prove advantageous when retaining the storage at an optimal inclination angle is not feasible. For instance, when the storage system is installed beneath a solar panel, the collector's angle may not remain stationary and could vary with the sun's movements.

In such circumstances, the flexibility of the inclination angle becomes a crucial factor in maximizing power storage, rendering Cases II and III preferable. This adaptability enables an energy-harvesting system to be effective even when environmental factors, such as the sun's position, continuously change. In order to design optimal energy systems, it is essential to comprehend the energy storage behavior under varying inclination angles, as demonstrated in these instances.

Fig. 14 compares the MVF and the total stored energy for the entire

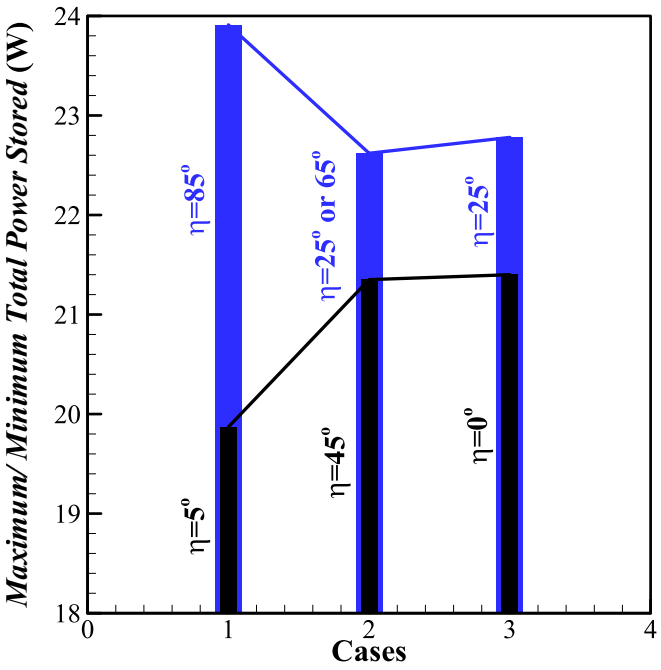

Fig. 13. A comparison among three cases: blue and black bars are the maximum and minimum values for total power stored.

melting process. The results are plotted for the best and worst inclination angles of the three configurations (Cases I-III). Case I, at an inclination angle of 85°, provides the highest MVF and total stored energy at all times. An inclination angle of 5° provides a fair MVF and energy storage at the initial and middle stages of the melting process, but its advantage drops at the final times. Therefore, the configuration of Case I could provide a fair storage power regardless of the inclination angle up to 80 % of storage capacity. However, charging >80 % depends on the inclination angle.

Configuration Case II is generally independent of the inclination angle over the entire melting process, but it provides the minimum MVF and stored energy compared to other cases. Case III delivers MVF and stored energy between cases I and II, and the melting behavior is also inclination angle-dependent. The optimum charging power for Case I ($\eta = 85°$) is about 5 % higher than the optimum for Cases II and III. Moreover, for Case I, the optimum charging power ($\eta = 85°$) is about 16 % higher than the minimum charging power ($\eta = 5°$).

Here, the best inclination angles for Cases I-III were selected, and the effect of the mass fraction of nanoparticles on the thermal energy storage of the enclosure was investigated. In this regard, Figs. 15 and 16 show the impact of mass fractions of nanoparticles on the MVF and total stored energy. Interestingly, a low mass fraction of nanoparticles (0.5 % wt) shows a minimal impact on both MVF and stored energy. However, as the mass fraction increases to 1 % and more, the trend of the results changes.

For Case I, both mass fractions of 1 % and 3 % show almost similar MVF time history, and the presence of nanoparticles significantly accelerated the melting process. The nanoparticles do not participate in melting and latent heat thermal energy storage, and hence, the presence of the nanoparticles reduces the heat capacity of the enclosure. As mentioned, the MVF time history of 1 % and 3 % wt were almost the same, but the energy storage for 3 % wt is much lower than 1 % wt due to the presence of GNP and the reduction in latent heat capacity of GNP-PCM. Thus, it can be concluded that 1 % wt GNPs is the best practice for dispersing nanoparticles to the PCM.

Fig. 16 shows that 1 % wt and 3 % wt produce almost the same MVF for Case II, but the stored energy for 3 % wt is much lower than 0 % wt. Thus, using 3 % wt GNP is not beneficial to thermal energy storage and the total capacity of the enclosure. However, using 1 % wt nanoparticles produces fair total energy storage with a drawback of a decrease in the total energy storage capacity of the enclosure.

Finally, the MVF for 3 % wt is slightly higher than 1 % wt for Case III (Fig. 17). Thus, considering the reduction in latent heat capacity of GNP-PCM with 3 % wt, the curves of thermal energy storage for 0 % wt and 3 % wt are the same. However, the curve ends much sooner for 3 % wt since the enclosure's overall thermal energy storage capacity is much lower in the presence of nanoparticles. Similar to Case I (Fig. 15), when 1 % wt, the curve of total stored energy is above all other curves, which shows a better rate of energy storage. However, it also should be noted that this curve stops before cases 0 % wt and 0.5 % wt, which indicates a lower overall heat capacity in the enclosure.

5. Conclusion

The impact of heating boundary conditions and inclination angle was investigated on the thermal charging of an enclosure filled with nano-

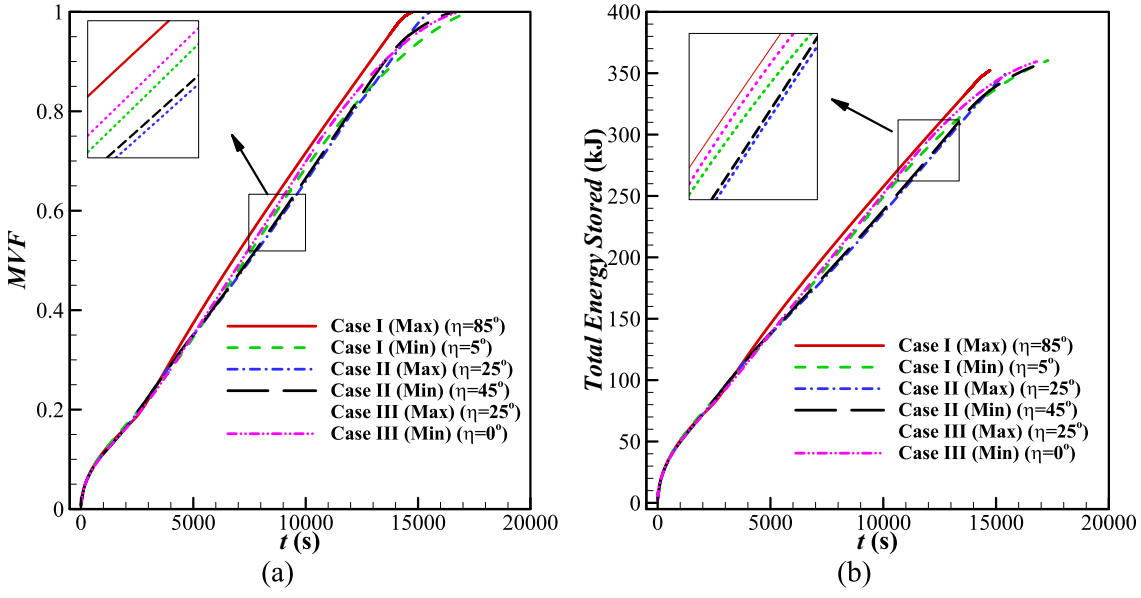

Fig. 14. (a) Melting volume fraction and (b) Total energy stored, for the best and worst results of cases I-III.

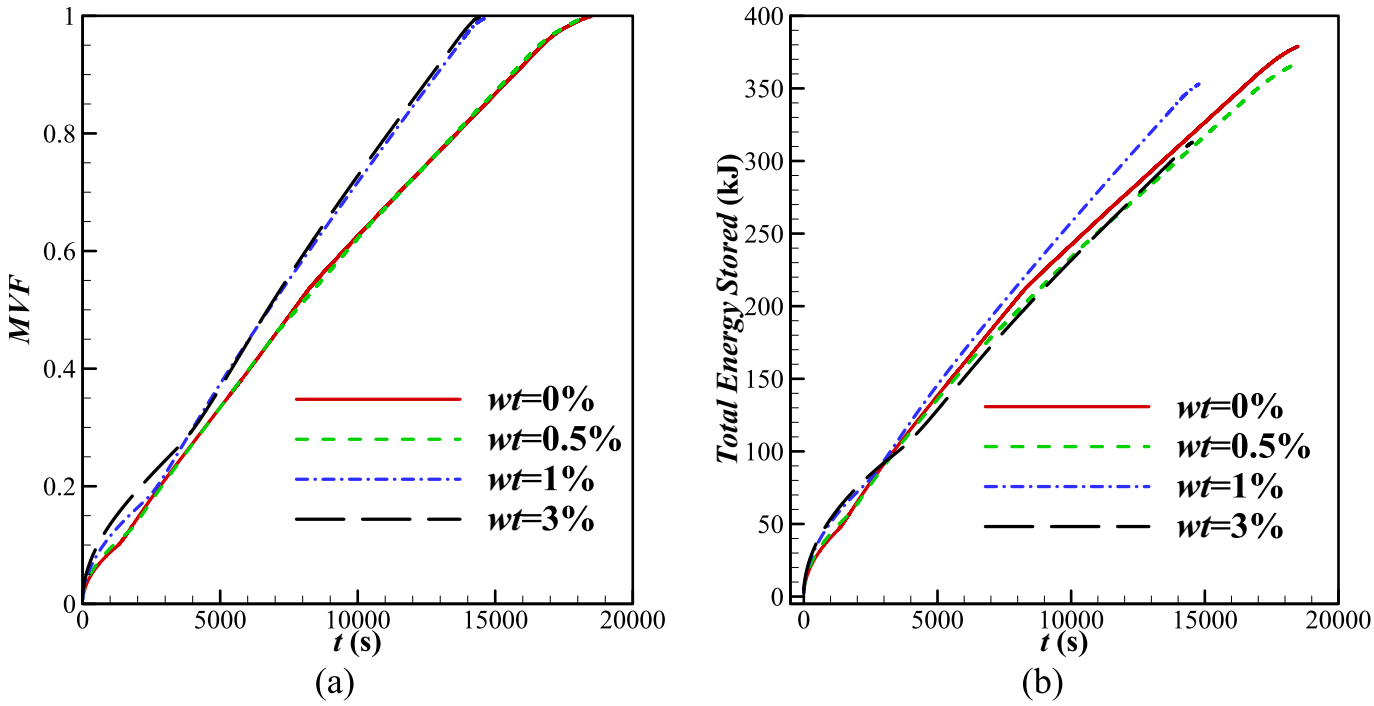

Fig. 15. Effect of weight fraction of the nanoparticles (*wt*) on the (a) Melting volume fraction and (b) Total energy stored for Case I.

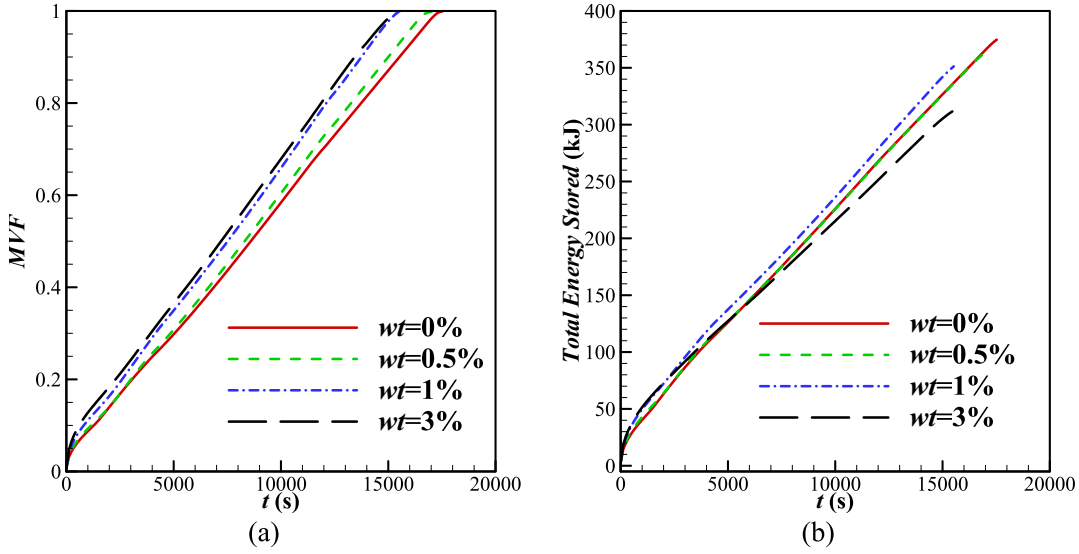

Fig. 16. Effect of weight fraction of the nanoparticles (*wt*) on the (a) Melting volume fraction and (b) Total energy stored for Case II.

enhanced PCM. The enthalpy-porosity technique, including the natural convection effects, was applied to model the phase change. Then, the finite element method was employed to solve the governing equations. Three partial heating boundary conditions were examined, and the thermal storage power was monitored. Considering the storage power, the best and worst inclination angles were found for 1 % wt GNP. Then, the impact of GNP concentrations on the melting volume fraction and thermal energy storage was studied. The main findings of the present research can be summarized as follows:

1- A combination of the heating location of the enclosure's walls and inclination angle could notably change the thermal charging behavior of the enclosure. Moreover, for each heating configuration, optimum charging powers were found.

2- For an enclosure heated from the side wall, Case I, the maximum charging power was found for an inclination angle of 85°. An inclination angle of 5° could lead to the minimum charging power. For an enclosure equally heated from the side wall and bottom (Case II), the inclination angles of 25° and 65° provide the maximum charging power. Finally, an enclosure mostly heated from the side wall (2/3) and partially heated from the bottom (1/3), Case III, produces the maximum charging power at 25°.

3- The charging power for Case I was notably greater than other cases at an optimum angle of 85°. However, the minimum charging power at an angle of 5° was much smaller than the minimum for two other cases. The charging power for the optimum angle ($\eta = 85°$) was 16 % higher than the minimum charging power at $\eta = 5°$.

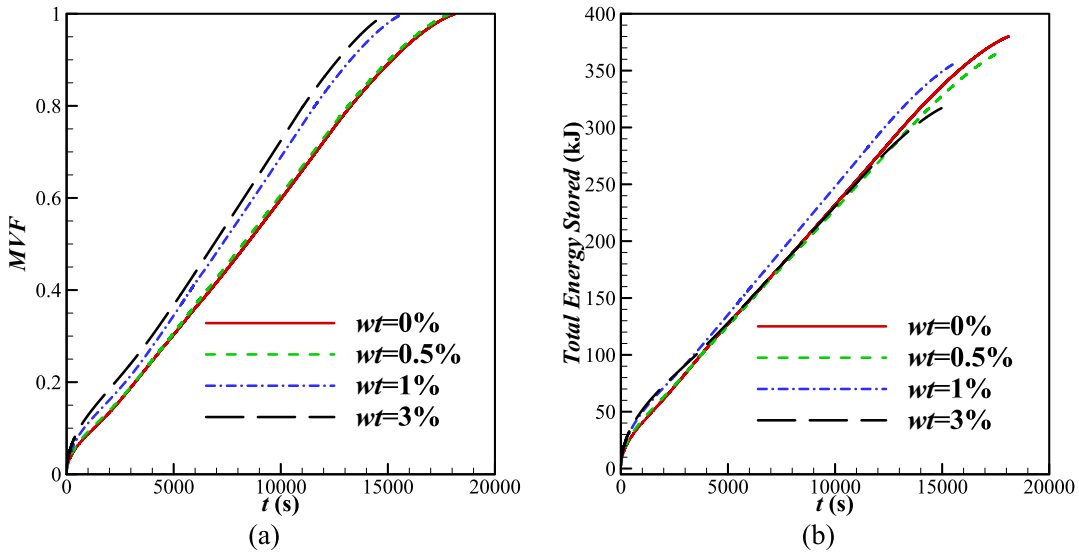

Fig. 17. Effect of weight fraction of the nanoparticles (*wt*) on the (a) Melting volume fraction and (b) Total energy stored for Case III.

4- Dispersing nanoparticles increases the melting rate but also decreases the heat capacity since the nanoparticles do not participate in latent heat energy storage. The results show that GPN with 1 % wt produces the maximum charging power. A higher concentration of nanoparticles (higher than 1%wt) decreases the total energy storage capacity and reduces the charging power. A low concentration of nanoparticles (lower than 1 % wt) cannot adequately enhance heat transfer.

CRediT authorship contribution statement

N. B. Khedher: Conceptualization, Methodology, Writing- Original draft preparation, Writing - Review & Editing. **M. Sheremet:** Conceptualization, Methodology, Software, Formal analysis, Data Curation. **A. M. Hussin:** Conceptualization, Validation, Investigation, Writing-Original draft preparation, Writing - Review & Editing. **S.A.M. Mehryan**: Investigation, Writing- Original draft preparation, Methodology, Writing - Review & Editing. **M. Ghalambaz:** Supervision, Methodology, Writing- Original draft preparation.

Declaration of competing interest

The authors declare that they have no known competing financial interests or personal relationships that could have appeared to influence the work reported in this paper.

Data availability

No data was used for the research described in the article.

Acknowledgment

This study is supported via funding from Prince Sattam bin Abdulaziz University project number (PSAU/2023/R/1444). This research of Mohammad Ghalambaz and Mikhail Sheremet was supported by the Tomsk State University Development Programme (Priority-2030).

References

[1] D. Zhang, S. Tian, D. Xiao, Experimental study on the phase change behavior of phase change material confined in pores, Sol. Energy 81 (2007) 653–660.
[2] H. Behi, M. Ghanbarpour, M. Behi, Investigation of PCM-assisted heat pipe for electronic cooling, Appl. Therm. Eng. 127 (2017) 1132–1142.
[3] S.K. Sahoo, M.K. Das, P. Rath, Application of TCE-PCM based heat sinks for cooling of electronic components: a review, Renew. Sust. Energ. Rev. 59 (2016) 550–582.
[4] J. Luo, D. Zou, Y. Wang, S. Wang, L. Huang, Battery thermal management systems (BTMs) based on phase change material (PCM): a comprehensive review, Chem. Eng. J. 430 (2022), 132741.
[5] N. Joshy, M. Hajiyan, A.R.M. Siddique, S. Tasnim, H. Simha, S. Mahmud, Experimental investigation of the effect of vibration on phase change material (PCM) based battery thermal management system, J. Power Sources 450 (2020), 227717.
[6] Q. Gu, G. Li, Z. Wu, The analysis on the battery thermal management system with composite phase change materials coupled air cooling and fins, J. Energy Storage 56 (2022), 105977, https://doi.org/10.1016/j.est.2022.105977.
[7] R. Chaturvedi, A. Islam, K. Sharma, A review on the applications of PCM in thermal storage of solar energy, Mater. Today: Proc. 43 (2021) 293–297.
[8] X. Xiao, P. Zhang, M. Li, Experimental and numerical study of heat transfer performance of nitrate/expanded graphite composite PCM for solar energy storage, Energy Convers. Manag. 105 (2015) 272–284.
[9] D. Zhou, G. Shire, Y. Tian, Parametric analysis of influencing factors in Phase Change Material Wallboard (PCMW), Appl. Energy 119 (2014) 33–42.
[10] M. Jaworski, Thermal performance of heat spreader for electronics cooling with incorporated phase change material, Appl. Therm. Eng. 35 (2012) 212–219.
[11] S. Mousavi, M. Siavashi, A. Zadehkabir, A new design for hybrid cooling of Li-ion battery pack utilizing PCM and mini channel cold plates, Appl. Therm. Eng. 197 (2021), 117398.
[12] X.-H. Yang, S.-C. Tan, Y.-J. Ding, L. Wang, J. Liu, Y.-X. Zhou, Experimental and numerical investigation of low melting point metal based PCM heat sink with internal fins, Int. Commun. Heat Mass Transf. 87 (2017) 118–124.
[13] J. Xie, H.M. Lee, J. Xiang, Numerical study of thermally optimized metal structures in a Phase Change Material (PCM) enclosure, Appl. Therm. Eng. 148 (2019) 825–837.
[14] C. Ji, Z. Qin, Z. Low, S. Dubey, F.H. Choo, F. Duan, Non-uniform heat transfer suppression to enhance PCM melting by angled fins, Appl. Therm. Eng. 129 (2018) 269–279.
[15] C. Zhao, M. Opolot, M. Liu, F. Bruno, S. Mancin, K. Hooman, Numerical study of melting performance enhancement for PCM in an annular enclosure with internal-external fins and metal foams, Int. J. Heat Mass Transf. 150 (2020), 119348.
[16] M. Esapour, A. Hamzehnezhad, A.A.R. Darzi, M. Jourabian, Melting and solidification of PCM embedded in porous metal foam in horizontal multi-tube heat storage system, Energy Convers. Manag. 171 (2018) 398–410.
[17] M. Iasiello, M. Mameli, S. Filippeschi, N. Bianco, Metal foam/PCM melting evolution analysis: orientation and morphology effects, Appl. Therm. Eng. 187 (2021), 116572.
[18] Z. Ma, W. Lin, M.I. Sohel, Nano-enhanced phase change materials for improved building performance, Renew. Sust. Energ. Rev. 58 (2016) 1256–1268.
[19] K.Y. Leong, M.R.A. Rahman, B.A. Gurunathan, Nano-enhanced phase change materials: a review of thermo-physical properties, applications and challenges, J. Energy Storage 21 (2019) 18–31.
[20] C. Yadav, R.R. Sahoo, Effect of nano-enhanced PCM on the thermal performance of a designed cylindrical thermal energy storage system, Exp. Heat Transf. 34 (2021) 356–375.
[21] R. Kalbasi, M. Afrand, J. Alsarraf, M.-D. Tran, Studies on optimum fins number in PCM-based heat sinks, Energy 171 (2019) 1088–1099.
[22] J.M. Mahdi, E.C. Nsofor, Multiple-segment metal foam application in the shell-and-tube PCM thermal energy storage system, J. Energy Storage 20 (2018) 529–541.

[23] M.Y. Yazici, M. Avci, O. Aydin, Combined effects of inclination angle and fin number on thermal performance of a PCM-based heat sink, Appl. Therm. Eng. 159 (2019), 113956.
[24] T. Bouzennada, F. Mechighel, T. Ismail, L. Kolsi, K. Ghachem, Heat transfer and fluid flow in a PCM-filled enclosure: effect of inclination angle and mid-separation fin, Int. Commun. Heat Mass Transf. 124 (2021), 105280.
[25] I. Al Siyabi, S. Khanna, T. Mallick, S. Sundaram, An experimental and numerical study on the effect of inclination angle of phase change materials thermal energy storage system, J. Energy Storage 23 (2019) 57–68.
[26] S. Huang, J. Lu, Y. Li, Numerical study on the influence of inclination angle on the melting behaviour of metal foam-PCM latent heat storage units, Energy 239 (2022), 122489.
[27] A.I.N. Korti, H. Guellil, Experimental study of the effect of inclination angle on the paraffin melting process in a square cavity, J. Energy Storage 32 (2020), 101726, https://doi.org/10.1016/j.est.2020.101726.
[28] B. Kamkari, H. Shokouhmand, F. Bruno, Experimental investigation of the effect of inclination angle on convection-driven melting of phase change material in a rectangular enclosure, Int. J. Heat Mass Transf. 72 (2014) 186–200.
[29] D. Chatterjee, N. Biswas, N.K. Manna, D. Kumar Mandal, A.J. Chamkha, Magneto-nanofluid flow in cylinder-embedded discretely heated-cooled annular thermal systems: conjugate heat transfer and thermodynamic irreversibility, J. Magn. Magn. Mater. 569 (2023), 170442, https://doi.org/10.1016/j.jmmm.2023.170442.
[30] N. Biswas, D.K. Mandal, N.K. Manna, A.C. Benim, Enhanced energy and mass transport dynamics in a thermo-magneto-bioconvective porous system containing oxytactic bacteria and nanoparticles: cleaner energy application, Energy 263 (2023), 125775, https://doi.org/10.1016/j.energy.2022.125775.
[31] N.K. Manna, N. Biswas, D.K. Mandal, U.K. Sarkar, H.F. Öztop, N. Abu-Hamdeh, Impacts of heater-cooler position and Lorentz force on heat transfer and entropy generation of hybrid nanofluid convection in quarter-circular cavity, Int. J. Numer. Methods Heat Fluid Flow 33 (2023) 1249–1286, https://doi.org/10.1108/HFF-07-2022-0402.
[32] Y. Pahamli, M.J. Hosseini, A.A. Ranjbar, R. Bahrampoury, Effect of nanoparticle dispersion and inclination angle on melting of PCM in a shell and tube heat exchanger, J. Taiwan Inst. Chem. Eng. 81 (2017) 316–334, https://doi.org/10.1016/j.jtice.2017.09.044.
[33] M. Shahabadi, B. Alshuraiaan, A. Abidi, O. Younis, M. Ghalambaz, S. Mehryan, Transient melting flow of a NePCM comprising GNPs in a semi-elliptical latent heat thermal energy storage unit, Int. Commun. Heat Mass Transf. 130 (2022), 105815.
[34] Z. Li, N. Hu, J. Tu, L. Fan, Experimental investigation of heat storage and heat transfer rates during melting of nano-enhanced phase change materials (NePCM) in a differentially-heated rectangular cavity, J. Therm. Sci. 29 (2020) 503–511, https://doi.org/10.1007/s11630-020-1225-2.
[35] A.J. Chamkha, A. Doostanidezfuli, E. Izadpanahi, M. Ghalambaz, Phase-change heat transfer of single/hybrid nanoparticles-enhanced phase-change materials over a heated horizontal cylinder confined in a square cavity, Adv. Powder Technol. 28 (2017) 385–397, https://doi.org/10.1016/j.apt.2016.10.009.
[36] S.A.M. Mehryan, M. Vaezi, M. Sheremet, M. Ghalambaz, Melting heat transfer of power-law non-Newtonian phase change nano-enhanced n-octadecane-mesoporous silica (MPSiO2), Int. J. Heat Mass Transf. 151 (2020), 119385, https://doi.org/10.1016/j.ijheatmasstransfer.2020.119385.
[37] Z.-Q. Zhu, M.-J. Liu, N. Hu, Y.-K. Huang, L.-W. Fan, Z.-T. Yu, J. Ge, Inward solidification heat transfer of nano-enhanced phase change materials in a spherical capsule: an experimental study, J. Heat Transf. 140 (2018).
[38] B. Kamkari, H.J. Amlashi, Numerical simulation and experimental verification of constrained melting of phase change material in inclined rectangular enclosures, Int. Commun. Heat Mass Transf. 88 (2017) 211–219.